

Thickness Dependence and Strain Effects in Ferroelectric Bi 2 FeCrO 6 Thin Films

Mircea V Rastei, Florian Gellé, Guy Schmerber, Alessandro Quattropani, Thomas Fix, Aziz Dinia, Abdelilah Slaoui, Silviu Colis

▶ **To cite this version:**

Mircea V Rastei, Florian Gellé, Guy Schmerber, Alessandro Quattropani, Thomas Fix, et al.. Thickness Dependence and Strain Effects in Ferroelectric Bi 2 FeCrO 6 Thin Films. ACS Applied Energy Materials, 2019, 2 (12), pp.8550-8559. 10.1021/acsaem.9b01465 . hal-02549988

HAL Id: hal-02549988
https://cnrs.hal.science/hal-02549988

Submitted on 5 Nov 2020

HAL is a multi-disciplinary open access archive for the deposit and dissemination of scientific research documents, whether they are published or not. The documents may come from teaching and research institutions in France or abroad, or from public or private research centers.

L'archive ouverte pluridisciplinaire **HAL**, est destinée au dépôt et à la diffusion de documents scientifiques de niveau recherche, publiés ou non, émanant des établissements d'enseignement et de recherche français ou étrangers, des laboratoires publics ou privés.

Thickness dependence and strain effects in ferroelectric Bi_2FeCrO_6 thin films

Mircea V. Rastei,*,† Florian Gellé,† Guy Schmerber,† Alessandro Quattropani,‡ Thomas Fix,‡ Aziz Dinia,† Abdelilah Slaoui,‡ and Silviu Colis*,†

†*Université de Strasbourg, CNRS, Institut de Physique et Chimie des Matériaux de Strasbourg (UMR 7504), 23 rue du Loess, BP 43, F-67034 Strasbourg Cedex 2, France*

‡*Université de Strasbourg, CNRS, Laboratoire des Sciences de l'Ingénieur, de l'Informatique et de l'Imagerie (UMR 7357), 23 rue du Loess, BP 20, F-67037 Strasbourg Cedex 2, France*

E-mail: mircea.rastei@ipcms.unistra.fr; colis@ipcms.unistra.fr

Abstract

We report on the ferroelectric properties of epitaxially grown Bi_2FeCrO_6 (BFCO) films with thicknesses of 7.5, 49 and 98 nm obtained by pulsed laser deposition. Because of the strains induced by the Nb-doped $SrTiO_3(001)$ substrate, the films exhibit a variable Fe-Cr order along the growth axis, with a disordered phase located near the interface and an increased order at the top of the films. This is first evidenced by X-ray diffraction and UV-visible-NIR absorption measurements as the ordered / disordered phases show different lattice parameters and band gaps. The strain effects which depend on the film thickness, are found to strongly impact on the ferroelectric properties. For the 49 nm thick film, piezoresponse force microscopy (PFM) reveals an out of plane intrinsic polarization orientation, effect which is absent for 98 nm thick films. The polarization anisotropy increases when reducing the thickness to 7.5 nm. The intrinsic polarization of the as-deposited 49 nm films induces a significant shift

of the current-voltage characteristics, demonstrating an I(V) hysteresis loop strongly weighted towards positive voltage values. The strain effects impact therefore on ferroelectric domains polarization. Conductive atomic force microscopy (C-AFM) carried out on poled areas, demonstrates a significant asymmetric current-voltage characteristics and an open circuit voltage up to 4.3 V for the 49 nm-thick sample which decreases to 1.2 V for the 98 nm thick one. These values are larger or at least comparable with the band gap of the ordered phase Bi_2FeCrO_6 phase (1.5 eV). Local current densities up to 20 A/cm^2 were measured by C-AFM under weak illumination, thus confirming the potential of Bi_2FeCrO_6 for ferroelectric solar cells.

Keywords: Ferroelectric oxides, PFM, C-AFM, Bi_2FeCrO_6, thin films, strains, clean energy, pulsed laser deposition

1 Introduction

Ferroelectric (FE) materials attract an increasing attention from the scientific community owing to their potential use in devices such as solar cells,[1,2] photodiodes[3] or ferroelectric random access memories.[4,5] The key property of these materials is related to their spontaneous electric polarization that can be switched by means of an external electric field. This polarization results from a non-centrosymmetric crystalline structure that generates a charge asymmetry inside the lattice. In the case of solar cells, these materials can replace the classic $p-n$ junctions since the charge separation can occur on the basis of their internal electric field. Another advantage of solar cells using such materials is that their open circuit voltage (V_{oc}) can exceed the one corresponding to the intrinsic bandgap and therefore their efficiency could be larger, at least theoretically, than the Shockley-Queisser limit.[6] Such large V_{oc} is a much sought-after effect, being first related to the existence of ferroelectric domain walls.[7] In this context, V_{oc} has been shown to depend on the distance between the electrodes and hence on the number of ferroelectric domain walls.[8,9] To the best of our knowledge no

photovoltaic effect has been observed in single domain FE samples.

Many of the above effects were observed on $BiFeO_3$, which became an emblematic material for photovoltaic studies. Although V_{oc} values of the order of tens of volts could be obtained in $BiFeO_3$-based solar cells under illumination, the efficiency of such cells remained remarkably small, generally below 1 %. For instance, among the best materials for FE solar cells only $BaTiO_3$ and PZT leaded to efficiencies of 0.6 % and 1.2 %, respectively.[10,11] In $BiFeO_3$ the small efficiency is due to the very poor overall conduction related to its large bandgap (around 2.7 eV).[12] In this respect, one solution to decrease the bandgap is to replace half of the Fe ions by Cr ones. Indeed, the Bi_2FeCrO_6 (BFCO) double perovskite shows a gap of only 1.4 eV in its ordered state that allowed obtaining junction-free simple and tandem solar cells with efficiencies of 3.3 and 8.1 %, respectively.[13] Note also that the gap can be modulated to some extent by controlling the Fe-Cr order,[14] resulting in a conversion efficiency that is dependent on the poling history.[2] In this context, the study of the polarization reversal in BFCO and the resulting electron conduction is essential to understand the mechanisms governing the energy conversion in solar cells or other ferroelectric applications.

The aim of this work is to study the influence of thickness and strains induced by the substrate on the ferroelectric polarization and conduction properties of Bi_2FeCrO_6 thin films grown by PLD on STO substrates. The study is carried out at microscopic scale using combined AFM, PFM and C-AFM analyzes. It is shown that in the first stages of the growth, BFCO is mostly disordered and the order improves while increasing the thickness. The compressive strain induced by the STO substrate has two impacts: i) is increasing the perpendicular anisotropy axis (visible in PFM images of thin films), and ii) generate an out of plane gradient of strain (i.e. gradient of electric field) which favors one of the out of plane polarization states. It is also shown that the two directions of polarization correspond to very different electric currents flowing across the layer. Interestingly, V_{oc} presents a large asymmetry for negative and positive polarization states, with absolute values that can exceed the band gap and which are highly dependent on the film thickness. Thus V_{oc} is not a simple

function of the distance between contacts (film thickness), but shows a much larger value (+4.3 V) for the 49 nm thick sample with respect to that (+1.2 V) obtained for the 98 nm film. The maximum current density at zero external bias measured by C-AFM is also remarkably high and reaches about 20 A/cm^2.

2 Experimental details

Bi_2FeCrO_6 films were deposited by pulsed laser deposition on Nb-doped $SrTiO_3$(001) substrates starting from in-house sintered targets and using a KrF excimer laser (248 nm). The films were grown at 750°C in O_2 atmosphere (10^{-2} mbar). The laser power and repetition rates were kept at 26 mJ and 2 Hz, respectively. The laser fluence on the target was about 1 J/cm^2. These conditions were found to minimize the concentration of antisite defects in the sample.[14] The films have thicknesses of 7.5, 49 and 98 nm, as determined from the X-ray reflectivity measurements (not shown here).

The crystalline structure of the samples was analyzed by X-ray diffraction using a Rigaku SmartLab diffractometer equipped with a Cu source and a Ge (220 × 2) crystal delivering the monochromatic Cu Kα_1 radiation (45 kV, 200 mA, 0.154056 nm). X-ray ϕ-scan analyzes were also performed in order to confirm the epitaxy of the films (not shown here; for details see ref.[14]). Rocking curves were recorded in order to perform a Williamson-Hall analysis[15] and extract the lateral coherence length and mosaicity of the films. Finally, reciprocal space mappings were recorded in order to evidence the strained structure of the Bi_2FeCrO_6 layer on the Nb-doped $SrTiO_3$(001) substrates.

The optical measurements of the films were investigated in the 200-1200 nm range using a Perkin-Elmer Lambda 950 spectrophotometer working in the ultraviolet-visible-near infrared (UV-Vis-NIR) range and equipped with an integration sphere.

The ferroelectric properties were investigated using the Piezoresponse Force Microscopy (PFM) and Conductive-Atomic Force Microscopy (C-AFM) techniques using a Bruker Icon

QNM microscope. All PFM images are recorded in the VPFM mode, by recording the phase shift of the cantilever with respect to the voltage excitation phase. A particular attention has been given to the measurement conditions in order to minimize other possible contributions (e.g. electrostatic, local Joule heating, electrostriction, etc) to the PFM signal.[16] Various supplementary tests (not shown here) have been performed in order to confirm the ferroelectric origin of the phase shift signal.[16] Namely, the dependence of the width of the hysteresis loop as a function of modulated V_{AC} voltage demonstrates a collapse of the cycle at a value corresponding to the coercive field.[17] Moreover, the frequency change of the modulation V_{AC} voltage from 1 to 50 kHz has also shown that the signal is largely independent on the probing frequency.[18] The tip was a 0.01-0.025 Ω·cm antimony n-doped Si covered with conductive diamond. For the results shown here, a 1.5 V AC voltage was applied to the sample at 40 kHz. The cantilever spring constant was 80 N/m. Such tips have a stable tip apex radius of about 50 nm. The normal loads were kept as low as possible (typically below 100 nN) in order to avoid tip-induced strain effects which can be intrusive into the PFM measurements.[19] Note that the rather large stiffness of the cantilevers (80 N/m) and the used applied normal forces also help avoiding the electrostatic contributions to the PFM signal which usually scales with the inverse of the contact stiffness.[20] The C-AFM experiments were conducted in the same load conditions, by measuring the electric current between the tip and the surface while applying a DC bias voltage on the sample with respect to the tip. It is important to already mention here, that this bias configuration is opposite to that used in PFM experiments, where the DC bias used to write poled areas is applied on the tip with respect to the sample. This detail is important when the I(V) curves and current maps are compared to the PFM written poled zones. The PFM signal, revealed here by the phase shift (and noted $\Delta\phi$), corresponds to the difference between the phase of the excitation AC voltage and the cantilever oscillation phase, measured when the tip is in contact with the surface.

3 Results and discussion

In order to understand the ferroelectric properties of Bi_2FeCrO_6, a thorough characterization of the structural and optical properties is required. BFCO presents a rhombohedral structure (R3 symmetry with $a_{rh} = 0.547$ nm and $\alpha_{rh} = 60.09°$) that can be approximated with a pseudcubic one ($a_{pc} = 0.3930$ nm). The equivalence is clearly evidenced in one of our previous works.[14] In the same work, using ϕ-scan measurements, we showed that the films, similar to the ones from the present work, exhibit a cube-on-cube epitaxial growth on $SrTiO_3(001)$ substrates (0.3906 nm)[21] according to the relation [100]BFCO(001)||[100]STO(001). Therefore, the X-ray diffractogramm recorded in $\theta - 2\theta$ configuration shows solely the $00l$ plane families of the BFCO and STO structures. No spurious phases could be detected in the detection limit of the XRD technique. In the present work, the BFCO peaks are clearly visible for the 49 and 98 nm thick samples, while for the 7.5 nm sample the diffraction peaks are absent. For a better visibility of the peaks a zoom on the diffractogramms around the 003 and 004 peaks of BFCO and STO is shown in fig. 1a. As expected, at such high angles, the BFCO peaks are clearly visible and located at the left of the STO peaks, as the BFCO (pseudocubic) lattice parameter is slightly larger with respect to that of STO. More interestingly, the BFCO peaks seem to be constituted of two components. Indeed, the BFCO(003) peak centered at 71.27° is constituted of two lines, L1 and L2, positioned at 71.02° and 71.54°, respectively. A similar observation can be also made on the BFCO(004) peak. It is important to note that the ratio of the intensities of these peaks is changing with the film thickness. If the intensity ratio L2/L1 is larger than 1 for the 49 nm thick film, this ratio is close to 1 for the 98 nm sample. It is also known that BFCO structure easily accepts antisite defects between Fe and Cr ions, as their size and valences are very close.[22] Due to compressive strains from the substrate, the growth of epitaxial ordered phases can be difficult, so that relaxation occurs through the appearance of different or disordered phases with close structure and parameters to those of the substrate and final ordered film phases. Such behavior is already known in the literature and often difficult to easily evidence by X-ray

diffraction.[23] It is therefore fair to assume that the L2 line corresponds to Fe-Cr disordered BFCO while the L1 line to the ordered phase that is obtained at large thicknesses upon strain relaxation. Note that a similar conclusion was also drawn by Nechache *et al* for BFCO films deposited on Si substrates.[24] This assumption will be further confirmed by the UV-visible absorption spectroscopy measurements presented further in this work. Finally, note that the L2 line (and its corresponding line at 104.2°), attributed to the Fe-Cr disordered phase (close to the substrate) shifts slowly towards smaller angles while increasing the thickness from 49 to 98 nm, suggesting a relaxation of the lattice parameter.

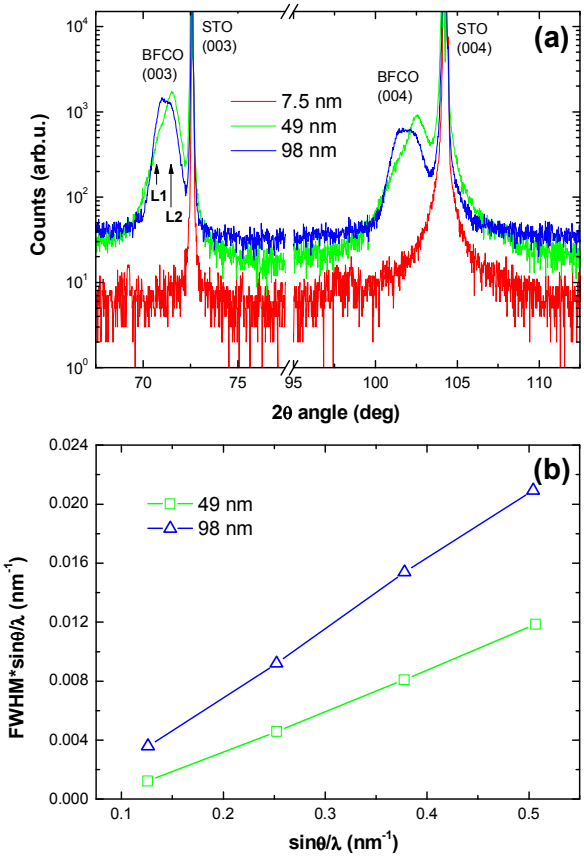


Figure 1: (a) X-ray diffraction patterns of Bi_2FeCrO_6 films with thicknesses of 7.5, 49 and 98 nm. Zoom on the (003) and (004) BFCO peaks. The BFCO peaks are constituted of two lines, L1 and L2, attributed to Fe-Cr ordered and disordered BFCO phases, respectively. (b) Williamson-Hall plot showing the broadening of the rocking curves recorded on the (001), (002), (003) and (004) reflections on the 49 and 98 nm thick samples.

The mosaicity (tilt angle η) and the lateral coherence length ($L_{\parallel}$) of the BFCO layers

were determined from the broadening of the rocking curves (not shown here) of the (001), (002), (003) and (004) reflections of BFCO. The Williamson-Hall analysis shows a rather linear variation of FWHM$\times$sinθ/λ (where FWHM is the full width at half maximum, i.e. the peak broadening) vs. sinθ/λ (fig. 1b). For the 49 and 98 nm thick layers the mosaicity is lower than 0.2° while the coherence length increases from 45 to 117 nm when increasing the film thickness. This suggests that the strains in the film relax progressively while increasing the thickness.

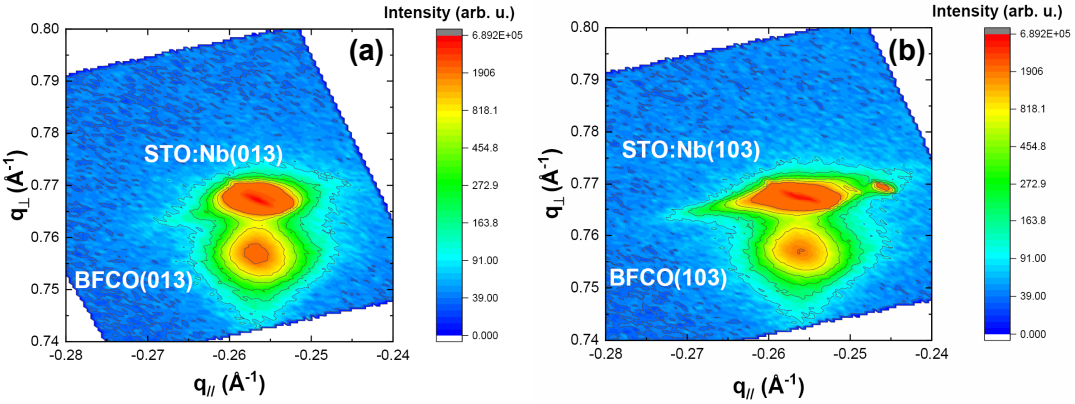


Figure 2: Reciprocal space maps (RSM) recorded on the (013) (a) and (103) (b) reflections of BFCO and Nb-doped STO.

In order to further show the existence of strains in our films, reciprocal space maps were recorded on a BFCO film showing only the Fe-Cr disordered phase (film deposited at 8 Hz for which Fe-Cr disorder is favored). The (013) and (103) reflections of BFCO and Nb-doped STO were used to determine the lattice parameters both in plane and along the growth axis (fig. 2). The c out of plane lattice parameters calculated from the two maps are of 0.3962(4) and 0.3963(4) nm while the in plane parameters are 0.3898(3) and 0.3906(2) nm. This result clearly show that the film is fully strained on the STO substrate (0.3906 nm).

Fig. 3 shows the Tauc plot of the BFCO films calculated from the absorption curves (inset of fig. 3) and assuming a direct band gap.[24] As it can be observed for the 98 nm thick sample, two slopes are observed for the $(\alpha h\nu)^2$ vs. energy variation, leading to two band gap values of 1.5 and 1.85 eV. These values can be attributed to the band gaps of ordered and

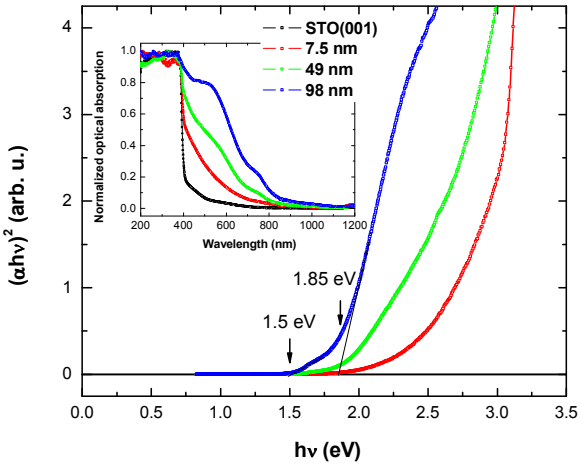


Figure 3: Tauc plots recorded Bi_2FeCrO_6 films with thicknesses of 7.5, 49 and 98 nm assuming a direct band gap. The inset shows the absorption spectra used to calculate the Tauc plots.

disordered BFCO, respectively.[2] Indeed, according to different studies, the band gap can be modulated by the deposition conditions which have a strong impact on the Fe-Cr order.[13,14] *Ab initio* calculations also show that the ordered structure has the smallest band gap.[14] While decreasing the thickness down to 49 nm, the component of the BFCO layer showing a gap at 1.5 eV becomes smaller and disappears completely for the thinnest 7.5 nm layer. This observation supports the XRD data and suggests that the L1 and L2 lines (fig. 1a) correspond to the ordered and disordered phases, respectively. Also note that the grain size can have an influence on the band gap. This is especially the case (and easily visible) when the grain size becomes smaller than about 20 nm and is generally attributed to quantum confinement effects (see e.g. ref.[25]). The result is a blueshift of the absorption edge. In our case the grain size is much larger (above 45 nm) which is due to the epitaxial character of the films. In such conditions, it is unlikely that the grain size can play a significant role.

Fig. 4a shows a contact mode AFM image measured on a BFCO film of 49 nm thickness. The image shows a height roughness below 5 nm and reveals a grained crystalline structure with a mean lateral grain size of about 150 nm. The surface impurity indicated by the arrow permits a clear identification of the area in both PFM (fig. 4b) and C-AFM images (presented further in this work). The simultaneously acquired PFM is shown in fig. 4b.

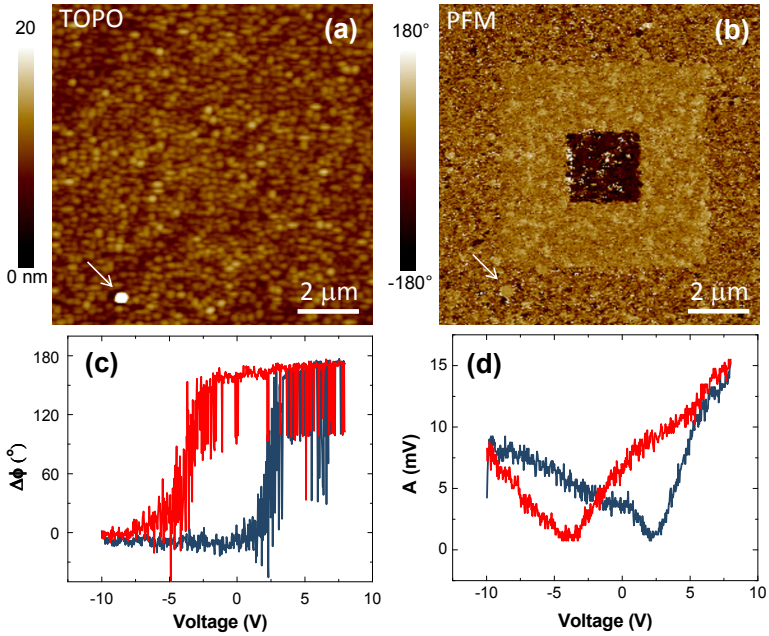


Figure 4: (a) AFM contact mode topography acquired simultaneously with (b) PFM phase-shift image (10×10 μm^2) recorded on a 49 nm thick BFCO film poled at V_t = +9 V in the large square, and at V_t = -5 V in the inner one. The large "bright" square was poled before switching in the opposite direction the "dark" area. The arrows show a surface impurity which is used for area identification. (c) Phase and (d) amplitude hysteresis loops as a function of the tip bias voltage. Blue curves correspond to forward (from negative to positive voltages), while red curves to a backward bias sweep.

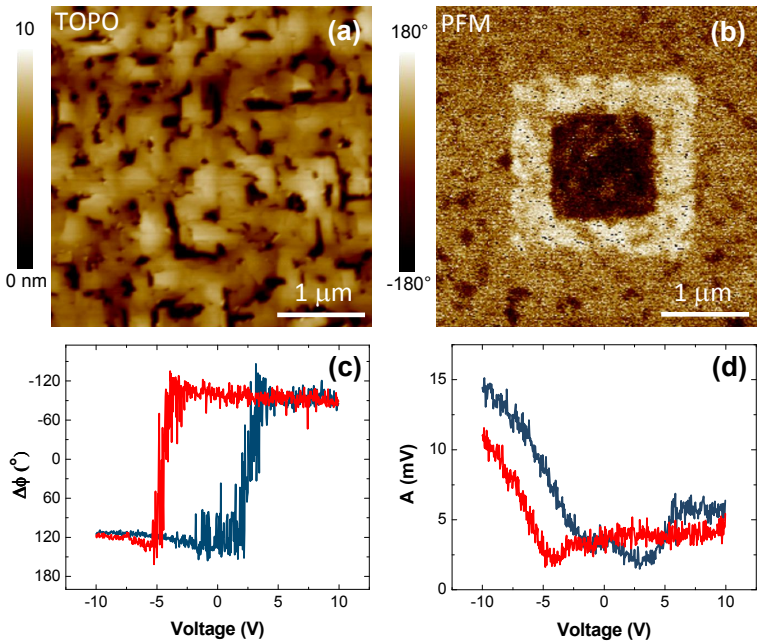


Figure 5: (a) AFM contact mode topography acquired simultaneously with (b) PFM phase-shift image (3×3 μm^2) carried out on the 98 nm thick BFCO film. (c) Phase and (d) amplitude hysteresis loops as a function of the tip bias voltage. Blue curves correspond to forward (from negative to positive voltages), while red curves to a backward bias sweep.

This image shows two poled domains of up (bright) and down (dark) electric polarizations. According to our poling conditions, a bright contrast in our PFM images corresponds to a positive voltage applied to the tip, which indicates that the film surface is negatively poled, hereafter referred to as negative polarization. Conversely, a dark contrast in the PFM images corresponds to a negative voltage applied to the tip, meaning that the film surface is positively poled (i.e. positive polarization).

Interestingly, as seen in fig. 4b, although the brighter squared area was written at $V_t = +9$ V, the contrast difference with respect to the unwritten zone (peripheral area), is rather small. Instead, the inner dark zone written at $V_t = +5$ V, reveals a far more pronounced PFM contrast difference with respect to the one measured on the peripheral unwritten zone. This indicates that the BFCO film presents an intrinsic polarization which, as revealed by the X-ray analyzes, can be understood in the light of a native compressive strain gradient induced by the substrate. This observation is central in this work and is of relevance for the I(V)

characteristics presented hereafter. It is interestingly to see that the phase-voltage hysteresis loops (fig. 4c), are in agreement with the PFM images, demonstrating a large open loop and close to 100 % remanent state. The simultaneously acquired amplitude hysteresis loop is shown in fig. 4d. It demonstrates that the surface modulation amplitude indeed passes by two minima at the coercive fields. In this hysteresis loop, there is a difference between the positive and negative coercive fields. It is then tempting to correlate this shift with the above contrast difference observed in the PFM images. As discussed in the following, such shifts in the phase-voltage hysteresis loops can be easily induced by many other factors, which cannot be systematically disentangled. Even in the absence of fatigue and aging effects, shifts of the PFM hysteresis loops with respect to the voltage axis may depend on the tip-surface contact, the precise spatial location, and normal load.[19,26,27] As the tip-surface contact area is very sensitive to local surface morphology, it is often encountered that hysteresis loops do not present the same coercive fields even for very close spatial locations. Along the same line, slightly different hysteresis loops can be induced by the grained structure of the films, which indeed compares with the tip size. We therefore restrain ourselves here to signals revealed in PFM images when discussing aspects related to intrinsic polarization effects.

In order to gain additional insights on the PFM contrast asymmetry, we performed similar experiments on a thicker film of 98 nm. First, as seen in fig. 5a, the topographic image shows a far more homogenous surface morphology, presenting larger and flatter crystalline grains. For comparison, the vertical color-coded scale is two times smaller than in fig. 4a. Second, the PFM image in fig. 5b, shows now that it is possible to write up and down domains of similar contrast difference with respect to the unwritten area. This suggests that the strain effect induced by the substrate decreases with the film thickness, as also indicated by X-ray analysis. The hysteresis loops from fig. 5c and d, show close to 100 % remanent states and coercive fields between 2.5 and 5 V. As for the thinner film described above, such a relatively large variation of the coercive field is induced by the grained structure. The exact coercive field is hence largely dependant on the precise nanoscale tip location on sample surface.

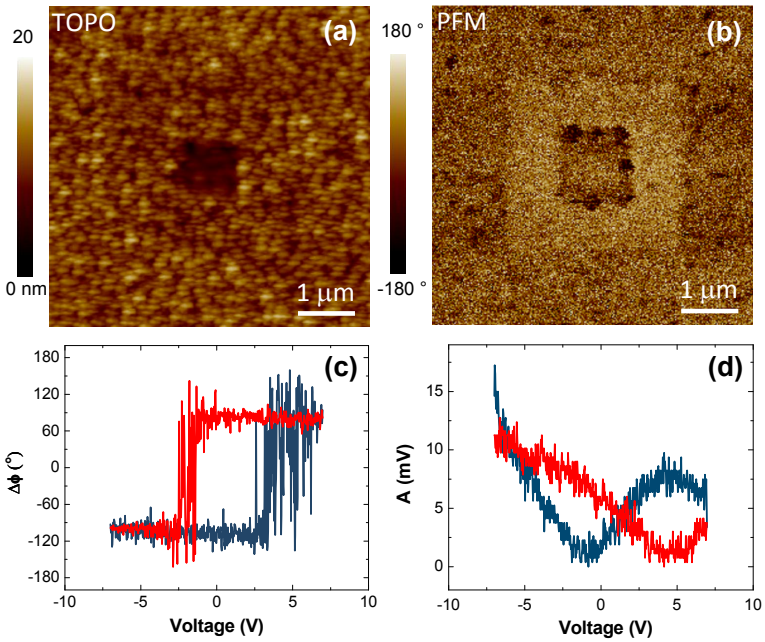


Figure 6: (a) AFM contact mode topography acquired simultaneously with (b) PFM phase-shift image (6×6 μm^2) carried out on the 7.5 nm thick BFCO film. (c) Phase and (d) amplitude hysteresis loops as a function of the tip bias voltage. Blue curves correspond to forward (from negative to positive voltages), while red curves to a backward bias sweep.

The topographic images for thinner films (7.5 nm) are in agreement with the above observations. As seen in fig. 6a, the surface morphology is formed by even smaller grains than for the 49 nm-thick films. Without correcting the convolution effects induced by the tip apex size, a raw estimation of the mean lateral size of the grains is about 100 nm. The vertical roughness is found to be about 5 nm, demonstrating that probably there are zones where such ultra-thin films are discontinuous. This aspect can interfere with the AFM imaging and the PFM contrast formation on poled areas. In general, a particular attention has been paid when such ultra-thin films were analyzed in PFM experiments, since the proximity of the substrate can not be longer neglected. The PFM image in fig. 6b, shows that, surprisingly, there is still some remanent polarization state, for both negative and positive written zones. This ferroelectric response is also found in the phase and amplitude hysteresis curves as seen in fig. 6c and d. Of importance, in the image from fig. 6b, the central square area, poled at V_t = -8 V, reveals some grains presenting a significant dark contrast (contrast close to the

one measured for the thicker films) while nearby, even if inside the written area, the contrast is almost absent, or at least of the same amplitude as for the unwritten part of the image.

These observations first speak in favor of a limited remanent states in the thinnest films. It is hence worth noting that for 7.5 nm-thick film the BFCO/Nb-STO interface is expected to impact to the largest extent the BFCO lattice. As a matter of fact, we recall that for the 49 nm-thick film, the PFM images revealed a bright contrast when negative charges accumulates at the topmost part of the film (because of the positive charges from the tip). This was precisely the polarization orientation which we show as being also intrinsically preferred by the film. It can then be deduced that the substrate-induced compressive strain favors positive charges at the bottom of the BFCO, i.e. interface in contact with the substrate.

This information is used here to explain why on 7.5 nm thick film, intense dark contrasts are observed only for some large grains, and moreover, why overall the PFM contrast in the inner square is similar with the one from unwritten area. Also, note that in the larger written square there is an overall clearer bright contrast. As the positive charges are favored at the bottom of the film, the reverse polarization (the one generating a dark contrast and involving negative charges at the bottom of the film) is indeed expected to be more easily achieved for larger grains because they extend further from the interface. This is precisely what is seen in the inner written square in the PFM image (fig. 6b). We therefore assume that the very thin parts of the film cannot sustain a remanent polarization which involves negative charges at the bottom of the film, an effect which is supported by the more present disordered phase revealed by the X-ray analyzes. In turn, a remanent polarization requiring positive charges at the interface is favored all over the film, explaining why "bright" domains sustain a remanent polarization state, as seen in the outer written square in fig. 6b. It is therefore important to recognize that such ultra-thin grained films are limit cases which may present significant differences with respect to a classical polarization effect as encountered in thick films.

It is also important to recall that charge screening and charge transfer effects brought

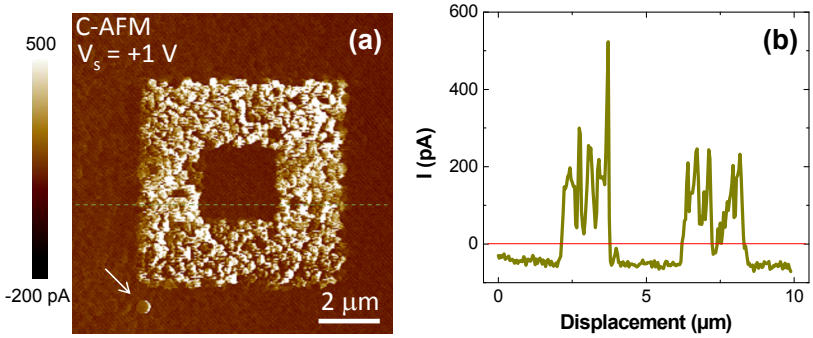


Figure 7: (a) C-AFM image (10×10 μm^2) and (b) line profile carried out on the 49 nm thick BFCO film. The scanned area is the same with the one presented in fig. 4 (see the feature pointed by the white arrow).

on by the conductive substrate, may also play a role in PFM contrast formation and/or on stabilization of the remanent state in ultrathin films. As the substrate is a far better conductor than the BFCO, a strain-favored accumulation of positive charges in a very thin BFCO film can easily be screened by the conduction electrons from the substrate. The resulting electric dipole moments are then expected to be very localized and have the same orientation as the polarization orientation induced by a negative voltage on the tip, i.e. as for the written dark contrast areas in the PFM images described above.

Another striking characteristic related to the variation of the BFCO thickness is given by local measurements of current-voltage I(V) curves, which were performed either by scanning poled areas as seen in fig. 7, or by keeping the tip in contact with the surface at a fixed position. For instance, fig. 7 shows a current mapping acquired at $V_S = +1$ V of the same poled area presented in fig. 4. It is seen that the current depends significantly on the polarization state of the film. In order to gain more insights into this behavior, we performed I(V) measurements with a fixed position of the tip while sweeping the sample voltage. Fig. 8 shows I(V) curves measured on 49 nm-thick sample, while sweeping the sample voltage V_S from -5 V to +8 V (blue lines) and back to -5 V (red lines). Complete I(V) curves are shown in fig. 8a, whereas a zoom near $V_S = 0$ is depicted in fig. 8b. There are three different curves acquired one after the other in the same conditions, in order to reveal the reproducibility of the curves and the fact that aging or irreversible surface modifications are

extraneous. Note however that although the I(V) curves may vary slightly from point to point, the signal is rather steady for a fixed tip position. An interesting result is that the I(V) curves present a significant asymmetry with respect to $V_S = 0$. Namely, the forward sweeping of V_S from -5 V to +8 V results in a positive open-circuit voltage (V_{oc}), while the sign is reversed for the backward voltage sweep. This is a clear indication that leaking currents are not significant,[28] in agreement with the rather compact AFM topographies of the films. By taking into account the coercive fields from fig. 4c, it becomes clear that the I(V) loop around $V_S = 0$ is created due to the switching of the BFCO polarization state. We recall again that in our case the bias voltage sign is reversed in PFM and in C-AFM experiments. For a positively poled surface, the V_{oc} and the short-circuit current (I_{sc}) are negative and positive, respectively. For a negative poling, the sign of V_{oc} and I_{sc} are inversed demonstrating a noteworthy switchable ferroelectric voltaic response. It is also worth mentioning that all I(V) curves were acquired without any external illumination (AFM in a closed box), although little diffusion from the red laser (670 nm) used for AFM cantilever deflection detection cannot be excluded. For this reason, we consider that all experiments are performed under a weak illumination, given by a spurious diffusion from the red detection laser of the AFM microscope.It is also perhaps important to recall here that due to the long range carrier mobility, the illumination is not absolutely necessary to be precisely under the tip. Nonetheless, the absolute values of V_{oc} and I_{sc} deserve a further attention. As seen in fig. 8b, there is an important difference between the absolute values of V_{oc} for positive and negative poled cases, as $V_{oc\uparrow}$ = -1.2 V and $V_{oc\downarrow}$ = +4.3 V, respectively. Instead, I_{sc} values are quite similar of 0.20 nA and 0.25 nA, respectively. Diode like behavior at the nanometer scale was already observed for other ferroelectric materials.[7,29] Without focusing on the I_{sc} values, very recently Zhang *et al*[29] indeed reported large variations of the current-voltage values between negatively and positively poled regions, results which are also consistent with previous works.[30] However, these studies have been realized by changing the bottom interface by inserting an additional $La_{0.67}Sr_{0.33}MnO_3$ layer between the substrate

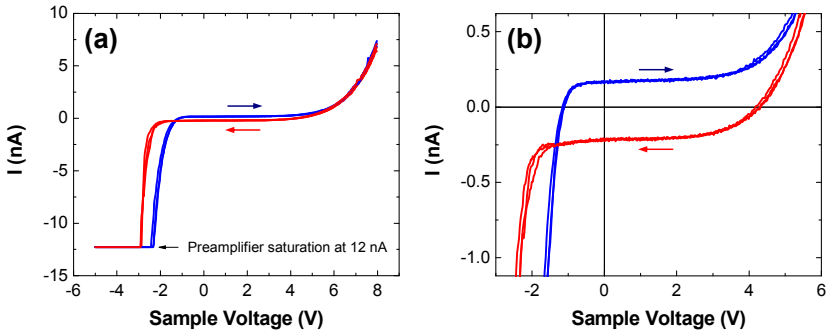


Figure 8: (a) Local I(V) hysteretic curves acquired in C-AFM mode on as prepared 49 nm-thick BFCO films. The blue curve is obtained while sweeping the voltage from -5 to +8 V. The red curve is obtained while sweeping back the voltage from +8 to -5 V. Three hysteresis curves are shown to reveal the high degree of reproducibility. Note the high hysteresis loop near voltage. (b) Zoom of the loops presented in fig. a.

and the ferroelectric film. In our case the bottom interface remains free of any additional layer and changes in the ferroelectric characteristics can then be investigated exclusively as a function of the ferroelectric film thickness. This allow us to gather conclusions relative to the modification of strain along the film thickness.

Fig. 9 shows the I(V) curves measured on the 98 nm-thick sample, while sweeping the sample voltage V_S from -5 V to +5 V (blue lines) and back to -5 V (red lines). In fig. 9a full I(V) curves are presented, whereas a zoom near $V_S = 0$ is shown in fig. 9b. The current variation also exhibits a hysteresis, again demonstrating an interesting switchable ferroelectric voltaic response. However, the behavior is very different when compared with the results obtained for the 49 nm-thick film. The most notable difference is a significant decrease of the V_{oc} values which falls now to +1.5 V (+4.3 V for 49 nm-thick sample).

As seen in fig. 9b, the overall shape of the hysteresis close to $V_S = 0$, is also changed, presenting now a two step variation occurring exclusively for the backward voltage sweep in the negative part of the sample voltage. Such a staircase switching mechanism is reminiscent of a polarization reversal taking place by sequential reversal mechanism, in relation with the larger thickness of the film, which, as previously discussed, impact the structural phases and strain relaxations. The other parameters are rather similar with those measured for the 49 nm-thick film. For instance, the V_{oc} is only slightly increased to -1.8 V (-1.2 V for the 49

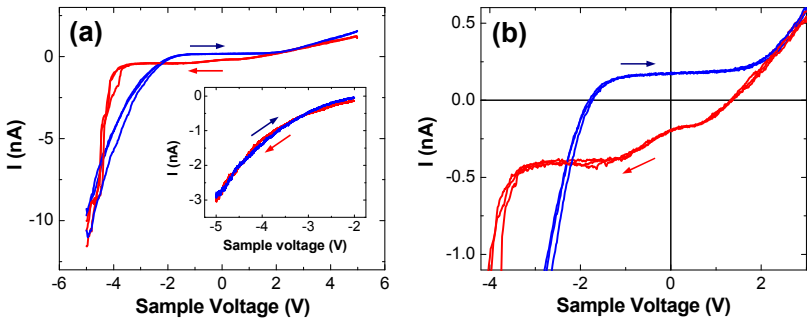


Figure 9: (a) Local I(V) hysteretic curves acquired in C-AFM mode on as prepared 98 nm-thick BFCO films. The blue curve is obtained while sweeping the voltage from -5 V to +5 V. The red curve is obtained while sweeping back the voltage from +5 V to -5 V. Three hysteresis curves are shown to reveal the high degree of reproducibility. Note the high hysteresis loop near voltage. The inset shows a minor hysteresis loop from -5 V to -2 V and back to -5 V. Note the absence of the hysteresis, as expected, if the sample voltage remains negative, i.e. sample remains positively poled. (b) Zoom of the loops presented in fig. a.

nm-thick film). The I_{sc} values also remained about 0.2 nA as those measured for the 49 nm-thick film. The inset from fig. 9a shows a minor I(V) loop, where V_S was swept from -5 V to -2 V and back to -5 V, thus remaining in the negative voltage regime. It is seen that the trace and retrace curves are almost identical, demonstrating, as expected, that the sample remains in the positive polarization state.

Using a tip-apex radius of 50 nm within the DMT model for contact mechanics[31] results in an upper limit estimation of the tip-surface contact area of 10^4 nm^2. The I_{sc} values hence, give a surprisingly high short-circuit current densities (J_{sc}) of about 20 A/cm^2, value that nevertheless agrees with previous findings on bismuth ferrite ($BiFeO_3$) ferroelectric films.[32] Note that this value is expected to increase in a quadratic way with the reduction of tip-surface contact radius, depending therefore on the sharpness of the tip and on contact continuity. However, as pointed out in ref.,[32] in the presence of light, photocurrents can instead be generated in a much larger area than the tip - sample contact because of the relatively slow ($1/r^2$) decrease of the electric field from the tip apex. Thus the collection area can be significantly higher as compared with the tip-surface contact. It is all the more remarkable than in our "dark" conditions, V_{oc} and J_{sc} give such a large values, which, as stated before, we interpret on the basis of strain gradients induced by the substrate. Again,

this conclusion is supported by the fact that the V_{oc} and J_{sc} values of the 98 nm-thick film are smaller that those on 49 nm-thick sample.

Previous works suggested that the increase of V_{oc} with the film thickness can be understood in terms of a larger number of ferroelectric domain walls crossed by the current paths. Another factor that may interfere with current-voltage characteristic is the contact properties, which can be more or less efficient and selective in the extraction of carriers.[33] However, in our case V_{oc} is four times larger in the 49 nm thick sample than in the 98 nm one. Although, we observed some deviations (less than 50 %) from these values, when placing the tip at different locations above the surface, this is nevertheless a clear indication that the polarization anisotropy (here induced by the strains) plays an essential role on the V_{oc} value. The larger V_{oc} obtained for the 49 nm thick sample can be understood if we consider that all polarization vectors are well aligned along the growth axis, i.e. perpendicular to the contacts. However, for the 98 nm thick film, these vectors are misaligned which can be easily evidenced by the multitude of phase contrasts that can be observed in fig. 5b. Finally, note that for the 49 nm thick sample a strong current density was observed (although enhanced by tip-effects[34]) of about 20 A/cm^2. If we keep in mind that the efficiency of a solar cell is proportional to the $V_{oc} \times J_{sc}$ product, it becomes obvious that in order to have a maximum conversion efficiency the polarization anisotropy and orientation are essential parameters that have to be considered. These parameters, as shown in the present work, can be tuned by strain engineering that should be considered for future high performance ferroelectric solar cell design.

4 Conclusion

Bi_2FeCrO_6 ferroelectric films with thicknesses of 7.5, 49 and 98 nm were obtained by PLD on Nb-doped $SrTiO_3$(001) substrates. Although the films are epitaxially grown, they present a large Fe-Cr disorder near the interface that is progressively reduced while increasing the

thickness. This is evidenced in the X-ray diffraction and UV-Visible-NIR absorption spectroscopy measurements that showed two BFCO($00l$) peaks on the diffractogramms and two absorption edges on the absorption spectra. The films show rather dissimilar surface roughnesses presenting different surface morphologies consisting of small grains for the thin films and to large (hundreds of nm) grains with flat topmost surfaces and edges oriented at 90° for the thick ones, reflecting an improved crystallinity. Ferroelectric nanodomains can be easily written and erased. For the 49 nm-thick film we evidenced a significant intrinsic polarization which is absent on the 98 nm-thick film. This strain-induced anisotropy induces a large V_{oc} of 4.3 V, much larger than expected from the band gap of Bi_2FeCrO_6. Surprisingly, this value decreases while increasing the film thickness, effect which is based on the reduced anisotropy and hence the misalignment of the polarization with respect to the growth direction. Electric current mapping on the written regions show a strong asymmetry of conduction with current densities that reach 20 A/cm^2. These results suggest that strain engineering is an essential key parameter for tuning V_{oc} and J_{sc} in solar cells and should be considered for increasing the conversion efficiency in ferroelectric-based devices. Our findings, eventually corroborated with an additional layer inserted at the substrate ferroelectric interface,[29] can constitute an extra route towards strain engineering of ferroelectric characteristics, both at the microscopic and macroscopic scales.

Acknowledgement

Authors are grateful to Gilles Versini for his help concerning sample preparation. This work was supported by the French Agence Nationale de la Recherche (ANR) under the reference ANR-11-LABX-0058-NIE within the Investissement d'Avenir program ANR-10-IDEX-0002-02. The work was carried out in the framework of the FERROPV project funded by the ANR under the reference ANR-16-CE05-0002-01. FG acknowledges the French Ministry of Education, Research and Innovation for financial support.

References

(1) Yang, M. M.; Kim, D. J.; Alexe, M. Flexo-photovoltaic effect. *Science* **2018**, *360*, 904-907.

(2) Quattropani, A; Makhort, A. S.; Rastei, M. V.; Versini, G.; Schmerber, G.; Barre, S.; Dinia, A.; Slaoui, A.; Rehspringer, J. L.; Fix, T.; Colis, S.; Kundys, B. Tuning photovoltaic response in Bi_2FeCrO_6 films by ferroelectric poling. *Nanoscale* **2018**, *10*, 13761-13766.

(3) Huang, W.; Chakrabartty, J.; Harnagea, C.; Gedamu, D.; Ka, I.; Chaker, M.; Rosei, F.; Nechache, R. Highly sensitive switchable heterojunction photodiode based on epitaxial Bi_2FeCrO_6 multiferroic thin films. *ACS Appl. Mater. Interfaces* **2018**, *10*, 12790-12797.

(4) Fujisaki, Y. Review of emerging new solid-state non-volatile memories. *Jpn. J. Appl. Phys.* **2013**, *52*, 040001.

(5) Garcia, V; Bibes, M. Inside story of ferroelectric memories. *Nature* **2012**, *483*, 279-281.

(6) Shockley, W.; Queisser, H. J. Detailed balance limit of efficiency of p-n junction solar cells. *J. Appl. Phys.* **1961**, *32*, 510-519.

(7) Choi, T.; Lee, S.; Choi, Y. J.; Kiryukhin, V.; Cheong, S. W. Switchable ferroelectric diode and photovoltaic effect in $BiFeO_3$. *Science* **2009**, *324*, 63-66.

(8) Yang, S. Y.; Seidel, J.; Byrnes, S. J.; Shafer, P.; Yang, C. H.; Rossell, M. D.; Yu, P.; Chu, Y. H.; Scott, J. F.; Ager III, J. W.; Martin, L. W.; Ramesh, R. Above-bandgap voltages from ferroelectric photovoltaic devices. *Nature Nanotech.* **2010**, *5*, 143-147.

(9) Seidel, J.; Fu, D.; Yang, S. Y.; Alarcón-Lladó, E.; Wu, J.; Ramesh, R.; Ager III, J. W. Efficient photovoltaic current generation at ferroelectric domain walls. *Phys. Rev. Lett.* **2011**, *107*, 126805.

(10) Zenkevich, A.; Matveyev, Y.; Maksimova, K.; Gaynutdinov, R.; Tolstikhina, A.; Fridkin, V. Giant bulk photovoltaic effect in thin ferroelectric $BaTiO_3$ films. *Phys. Rev. B* **2014**, *90*, 161409(R).

(11) Zheng, F.; Xin, Y.; Huang, W.; Zhang, J.; Wang, X.; Shen, M.; Dong, W.; Fang, L.; Bai, Y.; Shen, X.; Hao, J. Above 1% efficiency of a ferroelectric solar cell based on the $Pb(Zr,Ti)O_3$ film. *J. Mater. Chem. A* **2014**, *2*, 1363-1368.

(12) Ji, W.; Yao, K.; Liang, Y. C. Bulk photovoltaic effect at visible wavelength in epitaxial ferroelectric $BiFeO_3$ thin films. *Adv. Mater.* **2010**, *22*, 1763-1766.

(13) Nechache, R.; Harnagea, C.; Li, S.; Cardenas, L.; Huang, W.; Chakrabartty, J.; Rosei, F. Bandgap tuning of multiferroic oxide solar cells. *Nature Photonics* **2015**, *9*, 61-67.

(14) Quattropani, A.; Stoeffler, D.; Fix, T.; Schmerber, G.; Lenertz, M.; Versini, G.; Rehspringer, J. L.; Slaoui, A.; Dinia, A.; Colis, S. Band-gap tuning in ferroelectric Bi_2FeCrO_6 double perovskite thin films. *J. Phys. Chem. C* **2018**, *122*, 1070-1077.

(15) Williamson, G. K.; Hall, W. H. X-ray line broadening from filled aluminium and wolfram. *Acta Metall.* **1953**, *1*, 22-31.

(16) Vasudevan, R. K.; Balke, N.; Maksymovych, P.; Jesse, S.; Kalinin S. V. Ferroelectric or non-ferroelectric: Why so many materials exhibit "ferroelectricity" on the nanoscale. *Appl. Phys. Rev.* **2017**, *4*, 021302.

(17) Strelcov, E.; Kim, Y.; Yang, J. C.; Chu, Y. H.; Yu, P.; Lu, X.; Jesse, S.; Kalinin, S. V. Role of measurement voltage on hysteresis loop shape in piezoresponse force microscopy. *Appl. Phys. Lett.* **2012**, *101*, 192902.

(18) Seol, D.; Park, S.; Varenyk, O. V.; Lee, S.; Lee, H. N.; Morozovska, A. N.; Kim, Y. Determination of ferroelectric contributions to electromechanical response by frequency dependent piezoresponse force microscopy. *Sci. Rep.* **2016**, *6*, 30579.

(19) Lu, H.; Bark, C. W.; Esque de los Ojos, D.; Alcala, J.; Eom, C. B.; Catalan, G.; Gruverman, A. Mechanical writing of ferroelectric polarization. *Science* **2012**, *336*, 59-61.

(20) Kalinin, S. V.; Bonnell, D. A. Imaging mechanism of piezoresponse force microscopy of ferroelectric surfaces. *Phys. Rev. B.* **2002**, *65*, 125408.

(21) Gellé, F.; Chirita, R.; Mertz, D.; Rastei, M. V.; Dinia, A.; Colis, S. Guideline to atomically flat TiO_2-terminated $SrTiO_3$(001) surfaces. *Surf. Sci.* **2018**, *677*, 39-45.

(22) Shabadi, V.; Major, M.; Komissinskiy, P.; Vafaee, M.; Radetinac, A.; Baghaie Yazdi, M.; Donner, W.; Alff, L. Origin of superstructures in (double) perovskite thin films. *J. Appl. Phys.* **2014**, *116*, 114901.

(23) Moubah, R.; Colis, S.; Ulhaq-Bouillet, C.; Dinia, A. Defects analysis at the nanometric scale in $Ca_3Co_4O_9$ thin films. *Appl. Phys. Lett.* **2010**, *96*, 041902.

(24) Nechache, R.; Huang, W.; Lia, S.; Rosei, F. Photovoltaic properties of Bi_2FeCrO_6 films epitaxially grown on (100)-oriented silicon substrates. *Nanoscale* **2016**, *8*, 3237-3243.

(25) Jain, A.; Arun, P. Influence of grain size on the band-gap of annealed SnS thin films. *Thin Solid Films* **2013**, *548*, 241-246.

(26) Hölscher, H.; Schirmeisen, A. Dynamic force microscopy and spectroscopy. *Advances in Imaging and Electron Physics* **2005**, *135*, 41-101.

(27) Haviland, D. B.; van Eysden, C. A.; Forchheimer, D.; Platz, D.; Kassa, H. G.; Leclère, P. Probing viscoelastic response of soft material surfaces at the nanoscale. *Soft Matter* **2016**, *12*, 619-624.

(28) Xiao, J.; Chang, J.; Li, B.; Isikgor, F. H.; Wang, D.; Fan, Z.; Lin, Z.; Ouyang, J.; Zeng, K.; Chen, J. Room temperature ferroelectricity of hybrid organic-inorganic perovskites with mixed iodine and bromine. *J. Mater. Chem. A* **2018**, *6*, 9665-9676.

(29) Zhang, Q.; Rana, A.; Liu, X.; Valanoor, N. Electrode dependence of local electrical properties of chemical-solution-deposition-derived $BiFeO_3$ thin films. *ACS Appl. Electron. Mater.* **2019**, *1*, 154-162.

(30) Rana, A.; Lu, H.; Bogle, K.; Zhang, Q.; Vasudevan, R.; Thakare, V.; Gruverman, A.; Ogale, S.; Valanoor, N. Scaling behavior of resistive switching in epitaxial bismuth ferrite heterostructures. *Adv. Funct. Mater.* **2014**, *24*, 3962-3969.

(31) Derjaguin, B. V.; Muller, V. M.; Toporov, Y. P. Effect of contact deformations on the adhesion of particles. *J. Colloid Interface Sci.* **1975**, *53*, 314-326.

(32) Alexe, M.; Hesse, D. Tip-enhanced photovoltaic effects in bismuth ferrite. *Nature Comm.* **2011**, *2*, 256.

(33) Guerrero, A.; Garcia-Belmonte, G.; Mora-Sero, I.; Bisquert, J.; Kang, Y. S.; Jacobsson, T. J.; Correa-Baena, J. P.; Hagfeldt, A. Properties of contact and bulk impedances in hybrid lead halide perovskite solar cells including inductive loop elements. *J. Phys. Chem. C* **2016**, *120*, 8023-8032.

(34) Luo, Z. D.; Park, D. S.; Yang, M. M.; Alexe, M. Light-controlled nanoscopic writing of electronic memories using the tip-enhanced bulk photovoltaic effect. *ACS Appl. Mater. Interfaces* **2019**, *11*, 8276-8283.

Graphical TOC Entry

